Key Points:
- A mesoscale inversion ensemble is used to estimate CH_4 emissions in the LA basin
- Emission estimates are consistent with published observation-based estimates
- Oil and gas industries explain the differences between posterior and prior inventories

Correspondence to:
J. Brioude,
jerome.brioude@noaa.gov

Top-down estimate of methane emissions in California using a mesoscale inverse modeling technique: The South Coast Air Basin

Yu Yan Cui[1,2], Jerome Brioude[1,2,3], Stuart A. McKeen[1,2], Wayne M. Angevine[1,2], Si-Wan Kim[1,2], Gregory J. Frost[1,2], Ravan Ahmadov[1,2], Jeff Peischl[1,2], Nicolas Bousserez[4], Zhen Liu[5,6], Thomas B. Ryerson[1], Steve C. Wofsy[7], Gregory W. Santoni[7], Eric A. Kort[8], Marc L. Fischer[9], and Michael Trainer[1]

[1]Chemical Sciences Division, Earth System Research Laboratory, NOAA, Boulder, Colorado, USA, [2]Cooperative Institute for Research in Environmental Sciences, University of Colorado Boulder, Boulder, Colorado, USA, [3]Laboratoire de l'Atmosphere et des Cyclones, UMR8105, CNRS-Meteo France-Universite La Reunion, La Reunion, France, [4]Department of Mechanical Engineering, University of Colorado Boulder, Boulder, Colorado, USA, [5]Sandia National Laboratories, Livermore, California, USA, [6]Now at Ramboll Environ US Corporation, Novato, California, USA, [7]Department of Earth and Planetary Sciences, Harvard University, Cambridge, Massachusetts, USA, [8]Department of Atmospheric, Oceanic, and Space Sciences, University of Michigan, Ann Arbor, Michigan, USA, [9]Environmental Energy Technologies Division, Lawrence Berkeley National Laboratory, Berkeley, California, USA

Abstract Methane (CH_4) is the primary component of natural gas and has a larger global warming potential than CO_2. Recent top-down studies based on observations showed CH_4 emissions in California's South Coast Air Basin (SoCAB) were greater than those expected from population-apportioned bottom-up state inventories. In this study, we quantify CH_4 emissions with an advanced mesoscale inverse modeling system at a resolution of $8 \, km \times 8 \, km$, using aircraft measurements in the SoCAB during the 2010 Nexus of Air Quality and Climate Change campaign to constrain the inversion. To simulate atmospheric transport, we use the FLEXible PARTicle-Weather Research and Forecasting (FLEXPART-WRF) Lagrangian particle dispersion model driven by three configurations of the Weather Research and Forecasting (WRF) mesoscale model. We determine surface fluxes of CH_4 using a Bayesian least squares method in a four-dimensional inversion. Simulated CH_4 concentrations with the posterior emission inventory achieve much better correlations with the measurements ($R^2 = 0.7$) than using the prior inventory (U.S. Environmental Protection Agency's National Emission Inventory 2005, $R^2 = 0.5$). The emission estimates for CH_4 in the posterior, 46.3 ± 9.2 Mg CH_4/h, are consistent with published observation-based estimates. Changes in the spatial distribution of CH_4 emissions in the SoCAB between the prior and posterior inventories are discussed. Missing or underestimated emissions from dairies, the oil/gas system, and landfills in the SoCAB seem to explain the differences between the prior and posterior inventories. We estimate that dairies contributed 5.9 ± 1.7 Mg CH_4/h and the two sectors of oil and gas industries (production and downstream) and landfills together contributed 39.6 ± 8.1 Mg CH_4/h in the SoCAB.

1. Introduction

The average atmospheric mixing ratio of the greenhouse gas methane (CH_4) has increased by at least a factor of 2.5 since preindustrial times [*Myhre et al.*, 2013]. At current global concentrations, CH_4 is the second most important greenhouse gas behind CO_2 for anthropogenic radiative forcing. The atmospheric lifetime of CH_4 of ~12.4 years is much shorter than that of CO_2, but CH_4 has a significantly higher global warming potential than CO_2 (~86 times higher over 20 years and ~34 times higher over 100 years) [*Myhre et al.*, 2013, Table 8.7]. It has been argued that reducing emissions of CH_4 may be an important component of an initial strategy for avoiding the most severe impacts of global warming [*Alvarez et al.*, 2012; *Brandt et al.*, 2014].

Recently, many studies [*Pétron et al.*, 2012; *Brandt et al.*, 2014] found discrepancies in CH_4 inventories derived from bottom-up methods, based on an accounting of process-level activity and emission factors, and top-down approaches, which rely on atmospheric observations to infer emissions from a geographic region and often from a particular type of emissions source. Differences between bottom-up and top-down estimates suggest that the understanding of CH_4 sources is incomplete, leading to uncertainty in the application of regulations to mitigate CH_4 emissions.

Recent top-down approaches have shown that CH_4 emissions in the U.S. were underestimated in existing surface inventories [*Kort et al.*, 2008; *Miller et al.*, 2013; *Brandt et al.*, 2014], especially in the south-central U.S. and California. Greenhouse gas emissions in California have been regulated by the state legislature, which required that statewide greenhouse gas emissions be reduced to 1990 levels or lower by the year 2020. Recent studies have estimated CH_4 emissions both across California [*Jeong et al.*, 2012, 2013, 2014] and within the South Coast Air Basin (SoCAB) [*Wunch et al.*, 2009; *Wennberg et al.*, 2012; *Peischl et al.*, 2013] using either bottom-up inventory or top-down atmospheric approaches. The SoCAB region is particularly interesting because of the large population and known CH_4 sources from a densely populated urban area (Los Angeles) containing a large oil and natural gas production and distribution network, large landfills, and dairy livestock agriculture.

Bottom-up estimates of CH_4 emission in the SoCAB range from 26.2 Mg CH_4/h for NEI 2005 to 34.3 Mg CH_4/h for California Air Resources Board (CARB) 2009 (available at http://www.arb.ca.gov/cc/inventory/data/data. htm) and 61.6 Mg CH_4/h for Emission Database for Global Atmospheric Research version 4.2 (EDGARv4.2) (available at http://edgar.jrc.ec.europa.eu [*Rogelj et al.*, 2014]). One top-down technique to estimate CH_4 emissions uses observations of mixing ratios of coemitted or well-mixed species (CO and CO_2) and existing inventories of those species to infer CH_4 emissions. *Wunch et al.* [2009] estimated CH_4 emissions in the SoCAB using observed ratios of CH_4 mixing ratio with those of CO and CO2 from a ground-based Fourier transform spectrometer and found that CH_4 emissions in this area were 45.6 to 68.4 ± 11.4 Mg CH_4/h. *Wennberg et al.* [2012] and *Peischl et al.* [2013] used measurements on board the NOAA P-3 aircraft from the California Nexus, Research at the Nexus of Air Quality and Climate Change (CalNex) campaign in 2010 [*Ryerson et al.*, 2013] to infer SoCAB CH_4 emissions, taking advantage of P-3 flight plans designed for good spatial coverage over the basin. They used observed ratios between CH_4 and CO_2 or CO mixing ratios and their emission estimates from California Air Resources Board (CARB) to derive total CH_4 emissions from the SoCAB of 50.2 ± 11.4 and 46.7 ± 4.6 Mg CH_4/yr, respectively. The accuracy of this method is limited by (i) the accuracy of the surface emission estimates of the coemitted or well-mixed species (CO_2 and CO), and (ii) differences between the spatiotemporal emission patterns of CH_4 and the reference species. *Peischl et al.* [2013] also characterized the source attribution of CH_4 using CH_4 and light alkane measurements in the SoCAB and found that natural gas pipelines, geologic seeps, and the oil and gas industries accounted for most of the underestimation in current bottom-up CH_4 inventories.

Recently, an inversion method was applied to SoCAB CH_4 emissions by *Wecht et al.* [2014], using the adjoint of the Goddard Earth Observing System-Chemical (GEOS-Chem) model at $2/3° \times 1/3°$ resolution and prior emissions estimates from the EDGAR inventory. *Wecht et al.* [2014] estimated CH_4 emissions of 35.3 ± 9.1 and 47.9 ± 9.1 Mg CH_4/h using either GOSAT satellite or aircraft observations during the CalNex campaign, respectively. While the *Wecht et al.* [2014] CH_4 emission estimates agree with those of *Wennberg et al.* [2012] and *Peischl et al.* [2013], large uncertainties may arise from the coarse resolution of the GEOS-Chem model. The SoCAB region is associated with atmospheric mesoscale transport, such as land-sea breezes, and complex terrain, leading to impacts on the planetary boundary layer (PBL) and upslope transport, which influence pollution transport [*Angevine et al.*, 2013]. Hence, an inverse model at mesoscale should enable more confident estimates of the strength and spatial distributions of CH_4 emissions in the SoCAB region.

To tackle this problem, we use the off-line Lagrangian particle dispersion model FLEXible PARTicle-Weather Research and Forecasting (FLEXPART-WRF) coupled to three different Weather Research and Forecasting (WRF) model configurations to estimate source-receptor relationships and apply an inverse model at mesoscale. The mesoscale inverse system uses a Bayesian least squares method assuming lognormal distributions for the observations and the surface fluxes. Inverse models minimize the mismatch between measured and simulated observations of CH_4 concentrations by modifying surface flux densities from individual grid cells. The U.S. Environmental Protection Agency's (EPA's) National Emission Inventory (NEI) 2005 is used as a prior estimate of the CH_4 surface flux. Major sources of CH_4 in NEI 2005 include landfills and livestock but do not include oil and gas emissions. This inverse system has been used successfully to estimate CO, NO_y, and CO_2 in the SoCAB [*Brioude et al.*, 2013a]. Here we use the same inversion method to optimize surface emission fluxes of CH_4 with observations from six P-3 flights in May and June 2010 during the CalNex intensive field campaign. Section 2 presents the details of the methods used. The results are presented and discussed in section 3, followed by the conclusions of this work.
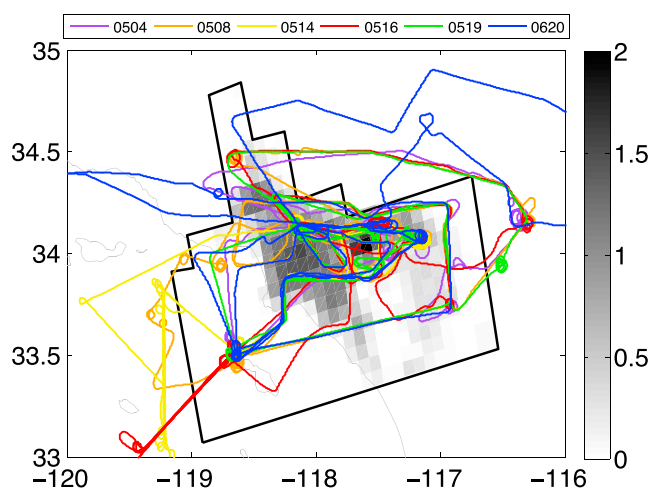
Figure 1. The prior inventory of CH_4 emissions from the U.S. EPA NEI 2005 (unit: $\mu g\,s^{-1}\,m^{-2}$) averaged at $8\,km \times 8\,km$ spatial resolution. Colored lines are flight tracks of six aircraft flights. The black line denotes the SoCAB domain.

2. Methods

2.1. Observations

The NOAA P-3 aircraft measured CH_4 mixing ratios over the SoCAB during CalNex 2010 [*Ryerson et al.,* 2013]. In our inverse modeling analysis of the CalNex campaign, we use six flights (4 May, 8 May, 14 May, 16 May, 19 May, and 20 June) to estimate CH_4 emissions in the SoCAB (Figure 1). These flights were dedicated to characterizing daytime emissions and chemistry in the area, focusing on late morning and afternoon periods after a well-mixed boundary layer was established. Vertical mixing at night is very uncertain 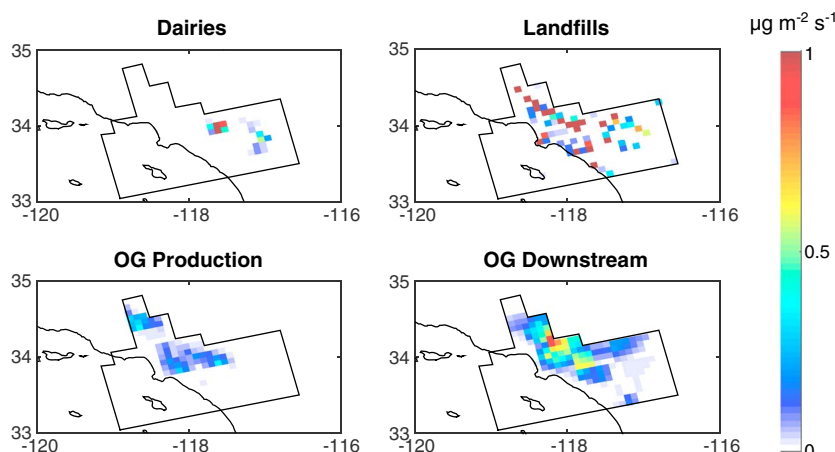in models and measurements, and therefore, nighttime data are not used in this study. Moreover, only observations in the boundary layer are used in the inversion, and we exclude the overwater segmentations of the 16 May flight because the models did not handle the boundary layer over the water properly [*Angevine et al.,* 2012]. No precipitation events were associated with these six flights.

On the research aircraft, CH_4 was measured once per second using wavelength-scanned cavity ring-down spectroscopy (WS-CRDS) by a Picarro 1301 m instrument [*Peischl et al.,* 2012, 2013]. The detailed information about WS_CRDS calibrations is described in section 2.1 of *Peischl et al.,* 2012. They estimated a total inaccuracy of CH_4 measurements of ±1.2 ppbv and reported a 1 s precision of ±1.4 ppbv during smooth flight and ±2.0 ppbv during turbulent flight. For 8 May, we use quantum cascade laser direct absorption spectroscopy (QCLS) measurements [*Kort et al.,* 2011], with an uncertainty of ±1 ppbv, as the Picarro instrument was not operating on this flight. The median difference between 1 s averaged QCLS and WS-CRDS was 4.5 (±5.1) ppb shown in Figure 13 of *Santoni et al.* [2014], which correspond to an error of 0.25% for measured CH_4 using 1800 ppb background.

The average flight speed was 100 m/s, and we use 30 s averaged values, equivalent to a horizontal resolution of ~3 km. The P-3 measurements in the SoCAB were collected close to the surface sources, and hence, chemical loss and soil sinks of CH_4 can be neglected. The uncertainty on simulated concentrations introduced by assuming CH_4 to behave as a passive tracer is lower than other sources of uncertainty pertaining to the simulation of atmospheric transport, such as those related to the errors in modeled wind field, PBL height, linear interpolations of the data, and turbulent mixing, estimated to be 20 to 30% in *Angevine et al.* [2014]. Therefore, we treat CH_4 as a passive tracer throughout the paper, regardless of the position of the measurements relative to the sources.

2.2. The Prior Emission Inventory

The $4\,km \times 4\,km$ EPA NEI 2005 v4 [*U.S. Environmental Protection Agency (EPA)*, 2015] is used to provide the prior emission inventory in the inverse system. CH_4 surface emissions from mobile on-road and off-road sources, nonpoint area sources, and point sources (negligibly small) are processed following EPA recommendations in the EPA SPECIATE 4.1 database [*Simon et al.,* 2010]. The $4\,km \times 4\,km$ NEI data are averaged onto the $8\,km \times 8\,km$ spatial resolution grid (Figure 1) used for the inverse modeling to relatively reduce the uncertainty with a loss of resolution. We do not include wetland and fire emissions because we consider them to be negligible contributors over the time period of our study. Emissions from oil and gas industries are very small in the NEI 2005.

It is expected that the limitations of the NEI 2005 inventory (underestimation of emissions from oil and gas industries and spatial distribution of sectors) will be compensated by the inversion method. Changes in spatial distribution in the posterior are discussed in section 3.2.

Figure 2. Methane emissions (unit: $\mu g\,m^{-2}\,s^{-1}$) in the SoCAB area (red box) from four sectors at $8\,km \times 8\,km$ spatial resolution: dairy, landfill, oil/gas production, and oil/gas downstream (storage, transmission, and distributions), with unit $\mu g\,m^{-2}\,s^{-1}$.

2.3. Spatial Distributions of Dairy, Landfills, and the Oil/Gas Industries

Dairy farms, landfills, and the oil and gas industries (production and distribution system) are known to be important sources in the SoCAB area [e.g., *Peischl et al.*, 2013]. Figure 2 shows their spatial distributions at $8\,km \times 8\,km$ resolution. Dairies and landfills are mapped using the same data as those shown in Figure 1c of *Peischl et al.* [2013]. The oil/gas production and downstream (including storage, transmission, and distribution) sectors are mapped using a hybrid inventory from Liu et al. (Mapping methane emissions from oil and natural gas systems in the contiguous United States, submitted to *Environmental Science and Technology*, 2015). Specifically, the spatially resolved emissions from oil and gas production are generated based on the 12 km gridded inventory of nonmethane hydrocarbons (NMHCs) for nonpoint oil and gas production sources from NEI-2011 and state-specific CH_4-to-NMHCs emissions ratios from *Eastern Research Group, Inc.* [2013]. Downstream oil and gas emissions from processing, storage, transmission, and distribution were from a spatial allocation of the national total emission from the EPA Greenhouse Gas Inventory [*EPA*, 2014] based on geospatial data of natural gas processing facilities, interstate and intrastate pipelines, compressor stations, and population density. The spatial distribution of those sectors in Figure 2 will be used to test independently the spatial distribution in the posterior and discuss CH_4 emissions per sectors. More discussion about these sectors is found in section 3.2.2.

2.4. Modeling

2.4.1. Trajectory and Meteorology

A three-dimensional Lagrangian dispersion model (FLEXPART) [*Stohl et al.*, 2005] was used to simulate hourly back trajectories along the flight tracks. High-resolution meteorological simulations were performed using the Weather Research and Forecasting (WRF) model [*Skamarock et al.*, 2005] to drive FLEXPART [*Brioude et al.*, 2013b]. In this study, FLEXPART-WRF version 3.1 served as our mesoscale atmospheric transport model to simulate contributions to airborne CH4 mixing ratios from surface CH4 fluxes, which has been used to constrain species such as CO, NO_x, and CO2 in airborne measurement-based inversions [*Brioude et al.*, 2013a].

Following *Brioude et al.* [2013a], we also consider three transport models. Uncertainties introduced by the transport models are, in part, taken into account in the inversion method and estimated in our results. The three transport models were designed using three different WRF meteorology configurations (Table 1). The first WRF configuration [*Angevine et al.*, 2012, 2013] (hereafter referred to as "WRF1") and the second WRF-Chem 3.1 configuration [*Kim et al.*, 2011; *Lee et al.*, 2011] (hereafter called "WRF2") have been previously evaluated and showed reasonable performance for scientific studies in the SoCAB [*Angevine et al.*, 2013]. WRF1 and WRF2 were used in *Brioude et al.* [2013a]. The third WRF configuration ("WRF3") is based on WRF-Chem version 3.4, with a nested horizontal grid at 4 km over California and 60 vertical levels. Global Forecast System/National Centers for Environmental Prediction (GFS/NCEP) data are used for the initial and boundary conditions to the WRF3 model. The Noah land surface model with the U.S. Geological

Table 1. Names and Configurations of the Three WRF Runs Used in This Study

Name	Version	Initialization	PBL Scheme	Grid Spacing (km)	Vertical Levels	LSM, Data	Wind Field
WRF1[a]	WRF 3.3	ERA-Interim	MYJ	4	60	Noah, UCM, MODIS	Time-averaged winds
WRF2[a]	WRF-Chem 3.1	ERA-Interim	YSU	4	60	Noah, UCM, USGS	Sigma dot ($\dot{\sigma}$) Winds
WRF3[b]	WRF-Chem 3.4	NCEP-GFS	YSU	4	60	Noah, USGS	Time-averaged winds

[a]The two configurations were used in *Brioude et al.* [2013a].
[b]The detailed description of WRF3.4 parameterizations can be found in http://www.mmm.ucar.edu/wrf/users/docs/user guide V3/contents.html.

Survey (USGS) land cover-land use and the Yonsei University (YSU) boundary layer scheme are used. WRF2 only provides the sigma dot (the derivative of WRF vertical coordinate with respect to time) instantaneous wind field while the other two provide time-averaged wind fields. We estimate correlations between the three WRF configurations and observations (Table S1 in the supporting information) of the entire CH_4 time series for the six flights analyzed during CalNex. The correlation coefficients between the three FLEXPART-WRF CH_4 time series are not much larger than the correlation coefficients between the measured CH_4 time series and simulated time series of each FLEXPART-WRF model. Therefore, each model can be considered as independent of the others in the sense that there is no correlation bias.

The Hanna scheme [*Stohl et al.*, 2005] is used in FLEXPART-WRF to prescribe a turbulent profile including both horizontal and vertical turbulences in the PBL. Time-averaged winds generated by the WRF model are used instead of instantaneous wind to reduce uncertainties in the Lagrangian trajectories in complex terrain [*Brioude et al.*, 2012]. PBL height, surface sensible heat flux, and friction velocity were taken directly from the WRF simulation. A total of 10,000 computational particles are released either every 30 s along the aircraft flight tracks or every 100 m during vertical profiles. No convection, chemical transformation, and deposition were simulated. FLEXPART simulates the trajectories over 24 h to focus on the local transport within the study area (i.e., the SoCAB). The trajectories are also limited to 24 h for computational feasibilities. Hence, the influence of previous-day transport and emissions is ignored, which will increase the uncertainty in the flux estimates. *Brioude et al.* [2013a] estimated that restricting the trajectories to 24 h added an uncertainty of ~7% to the surface emission estimates.

The FLEXPART-WRF output has a horizontal resolution of 8 km × 8 km, with 1 h output time interval. The output, also referred to footprint (in $s\,m^3\,kg^{-1}$), consists of a residence time within a surface layer (in meter) weighted by the atmospheric density, which represents the sensitivity of the airborne measurements to surface emissions. When combined with a surface emission inventory (in $kg\,m^{-2}\,s^{-1}$), one can calculate a mixing ratio for each set of trajectories along the aircraft flight track. In this way, FLEXPART-WRF linearizes the transport processes between the surface and the aircraft. This approach alleviates the need for an adjoint model of WRF-Chem (not currently available) in the application of the inversion technique [*Brioude et al.*, 2013a; *de Foy et al.*, 2015].

2.4.2. Inverse Modeling

We apply the inverse modeling approach described in *Brioude et al.* [2011, 2013a] to the CH_4 data collected in the SoCAB during CalNex. The observations used in the inverse modeling are the CH_4 mixing ratio enhancements above background. We define the background CH_4 for each flight as the lowest mixing ratio found in the atmospheric boundary layer below 2 km upwind of the SoCAB, which is also close to the value of the mode in the distribution of all mixing ratios measured below 2 km during the campaign. The enhancements in CH_4 are ~10% of background concentrations on average. The background concentration estimates were associated with an uncertainty of 10 ppb due to the variability in the low concentrations found in the PBL for each flight. This uncertainty was added to the measurement uncertainties in the inversion. Negative deviations from the background are removed from the observation data set and a small value of 10^-5 ppb was used instead.

To calculate the best estimates of CH_4 surface flux emissions, we use an iterative method to minimize a lognormal Bayesian least squares cost function with solutions in a median of the distribution, similar to the one used in *Brioude et al.* [2011]:

$$J = \frac{1}{2}(\ln(y_0) - \ln(Hx))^T R^{-1}(\ln(y_0) - \ln(Hx)) + \frac{1}{2}\alpha(\ln(x) - \ln(x_b))^T B^{-1}(\ln(x) - \ln(x_b)) \qquad (1)$$

where y_0 is the observation enhancement above the background value owing to surface emissions with the $p \times 1$ dimension and p is the number of observations. Parameter x is a $m \times 1$ vector of the posterior solutions and m is the number of gridded fluxes in space and time. H are the FLEXPART-WRF outputs, which construct a linear linkage between surface emissions and mixing ratios at given receptors, and the dimension of H is $p \times m$. Parameter x_b is a $m \times 1$ vector of prior fluxes, and R (dimension: $p \times p$) and B (dimension: $m \times m$) are error covariance matrices of observations and prior fluxes in the lognormal distribution space. Parameter α as a regularization parameter that comes from the L-shape criterion [*Henze et al.*, 2009], which is used to balance the errors in both covariance matrices to obtain the smallest sensitivity to the error in either the observations or the prior.

The advantage of using a lognormal transformation in the cost function is that no negative fluxes are found in the posterior so that we obtain a minimum variance solution (equivalent to the mean of the distribution) and not a likelihood, and the lognormal distribution follows more closely the observed CH_4 mixing ratios (after subtracting the background value). This approach avoids the drawbacks of other techniques used to prevent negative fluxes, such as modifying covariance matrices or bounded inverse methods [e.g., *Stohl et al.*, 2009; *Miller et al.*, 2014].

The observation errors, which include uncertainties from the measurements and from the background definition for each flight, typically, are assumed to be uncorrelated. Likewise, we assume that errors in the prior surface inventory are uncorrelated. Hence, the error covariance matrices of the observations (R) and prior (B) are modeled as diagonal matrices.

We use four time intervals to construct a four-dimensional (three spatial dimensions plus time) inversion following *Brioude et al.* [2013a]: (i) morning rush hours between 13:00 UTC and 16:00 UTC (06:00–09:00 local time), (ii) midday hours between 17:00 UTC and 21:00 UTC (10:00–14:00 local time), (iii) evening rush hours between 22:00 UTC and 01:00 UTC (15:00–18:00 local time), and (iv) nighttime hours between 02:00 UTC and 12:00 UTC (19:00–5:00 local time). The four time intervals are applied to both trajectories and prior emissions. The values reported in section 3 are the averages for the two time intervals between 17:00 UTC and 01:00 UTC (10:00–18:00 local time) when we have the strongest confidence in the transport models and therefore in the inversion.

Over the SoCAB domain, the Jacobian matrix H, representing the transport model in the inversion, has a dimension of 768 to 1109 rows (the total number of 30 s averaged observations in each individual flight) by 23280 columns (the total number of surface grid cells with four time intervals). To reduce the dimension of the matrix in order to obtain inversion solutions efficiently and to reduce cross correlations between surface fluxes in the posterior, we cluster surface grid cells in the domain using an optimality criterion based on the Fisher information matrix, which is different than *Brioude et al.* [2013a] that limited the inversion on grid cells with significant emission in the prior. Here we use a similar criterion as *Bocquet et al.* [2011] to construct adaptive grids in the control space:

$$\mathcal{J} = \mathrm{Tr}\left(BW^T R^{-1} W\right) \qquad (2)$$

where $\mathcal{J}$ is the criterion and W is the derivative of the Jacobian matrix H assuming a lognormal distribution. We classify the surface grid cells into clusters according to the neighbor method: namely, neighboring grid cells having similar values are aggregated as a cluster. In addition, grid cells with high values (e.g., equal to and above -5) of $\mathcal{J}$ are not aggregated. After applying this criterion, the domain in Figure 3, showing the control space of the inversion, uses 1201 clusters for each time interval, reducing the total grid cells in the inversion by a factor of ~5 (from 23,280) while mitigating information loss on surface fluxes.

For each flight and transport model, we used 100 iterations of the inversions with a random term (equivalent to a standard deviation of 5% of a lognormal distribution of prior flux estimates) to minimize cross correlation in the prior and hence in the posterior. The uncertainty in the posterior emission estimate from the ensemble of single-flight-based inversions is then estimated by using the posterior covariance matrix to estimate the posterior uncertainty for each realization and as the standard deviation of the distribution represented by the 1800 realizations from the ensemble of six flights and three transport models.

The uncertainty from the FLEXPART Lagrangian model cannot be assessed fully with this approach, but we assume that this uncertainty is small compared to the uncertainties in the meteorological fields [*Hegarty et al.*, 2013]. *Angevine et al.* [2014] evaluated the uncertainty in atmospheric transport to be 20 to 40% in a
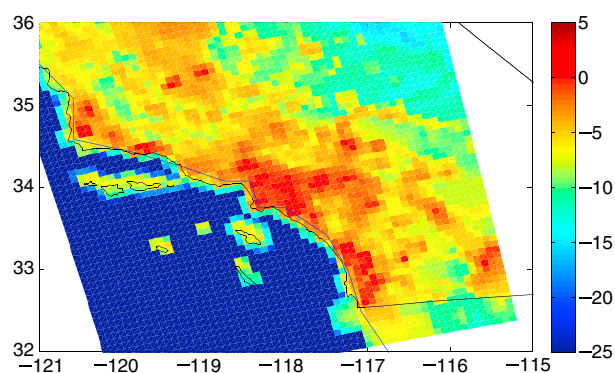
Figure 3. A map (log scale) of the Fisher information matrix criterion in the SoCAB based on the WRF1 transport model at a spatial resolution of 8 km × 8 km. See the text in section 2.4.2 for the details. Grid cells are aggregated into clusters when values of the criterion in adjacent cells are below −5. Cells with values equal to and above −5 are not aggregated. After aggregating, the original 5820 grid cells are aggregated into 1201, 1199, and 1200 clusters for the WRF1, WRF2, and WRF3 transport models, respectively.

FLEXPART-WRF ensemble of six WRF configurations due to uncertainties in meteorological fields. It is still unclear how this uncertainty propagates in the inversion system. However, our ensemble of only three WRF configurations might underestimate the uncertainty introduced by the FLEXPART-WRF simulated transport in the posterior estimates.

3. Results and Discussion

3.1. Posterior-Prior Differences in Emission Strengths

3.1.1. Total Emissions of CH_4

Back-trajectory footprints of the six flights from the three transport models are shown in Figure 4. The footprints provide a sense of the ability of the aircraft observations to constrain surface sources across the SoCAB.

The spatial distributions of footprints have similar patterns and emphasize the impact of northerly and northwesterly background airflow on the SoCAB domain. The six flights sampled predominantly downwind of the surface emissions in the SoCAB area.

The total posterior emissions for the SoCAB domain are calculated for each flight and for each transport model over the SoCAB area (Table 2 and Figure S1 in the supporting information). According to a recent report [*United States Energy Information Administration*, 2015], the seasonality of natural gas consumption in California had an amplitude of 15% in 2010. As seasonal variation in natural gas distribution leak is small [*McKain et al.*, 2015], one can assume a seasonality of 15% from NG leaks in Los Angeles. *Peischl et al.* [2013] found that 47% of total CH_4 emission in SoCAB was due to NG leaks. As the seasonality from Landfills and Dairies in the Los Angeles basin should be small, one can expect a seasonality of ~10% in the CH4 emission.

Diurnal and day to day variations in methane emission have been observed from feedlots [*Gao et al.*, 2011] and landfills. One can expect smaller emission variation from oil and gas facilities as their industrial activities have no particular diurnal variation. Finally, mobile sources, which have a strong diurnal profile, contribute only 1% of the total methane emission and should have a small impact. The six flights used in this study are not enough to fully cover the diurnal and day to day emission variations from landfills and feedlots, sources that contribute 44% to the total methane emissions in Los Angeles (LA) basin [*Peischl et al.*, 2013]. Hence, our posterior emission uncertainty estimates should be considered as a lower limit.
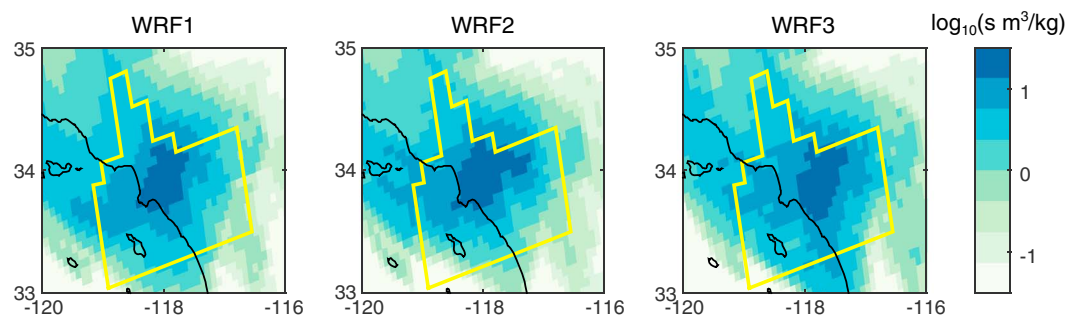

Figure 4. Averaged 1 day backward trajectory footprints with log scale for the six aircraft flights, based on each of the three WRF configurations, respectively. The yellow line shows the SoCAB domain. Footprints related to the overwater segments of the 16 May flight are excluded here.

Table 2. Total Emissions of CH_4 (Mg/h) Over SoCAB Derived From Each of the P-3 Flights With the Ensemble of Three Different Transport Models and an Averaged Estimate of CH_4 Emissions Based on Six Flights and Three Transport Models

Fight	4 May	8 May	14 May	16 May	19 May	20 June	Mean
Total emissions (Mg CH_4/h)	46.6 ± 10.6	46.9 ± 5.5	47.9 ± 10.1	47.8 ± 6.4	48.6 ± 11.2	39.9 ± 7.1	46.3 ± 9.2

The posterior values for the three transport models range from 45.1 to 48.2 Mg CH_4/h. The mean values over the six flights for each transport model are also shown in Figure S1. The three transport models' posterior estimates have a mean value 46.3 Mg CH_4/h with uncertainties of 21%, 19%, and 19%, respectively. Combining the three transport models, we estimate an optimized value of 46.3 ± 9.2 Mg CH_4/h for the SoCAB area (Figure 5 and Table 2). The uncertainty here includes the posteriors' uncertainty and the transport models' uncertainty.

Our estimate is higher by factor of ~1.8 than NEI 2005 (26.2 Mg CH_4/h). Our estimate is in agreement with previous estimates derived from observations taken over the same time period (Figure 5; 50.2 ± 11.4 Mg CH_4/h [*Wennberg et al.*, 2012], 46.7 ± 4.6 Mg CH_4/h [*Peischl et al.*, 2013], 31.9–44.5 Mg CH_4/h (Santoni et al., California's methane budget derived from CalNex P-3 Aircraft Observations and a Lagrangian transport model, submitted to *Journal of Geophysical Research*, 2014), and 47.9 ± 9.1 Mg CH_4/h [*Wecht et al.*, 2014]).

The precision and the accuracy of the surface flux estimates based on a single flight can also be evaluated. The total posterior emission estimates vary by ~6% between the six flights shown in Table 2. However, as mentioned above, the variation in posterior emission across the meteorological models is closer to 20% [*Angevine et al.*, 2014]. Hence, a given day surface emission estimates in the SoCAB can likely be estimated to within ~20% from a single flight's data and a single meteorological model for this summer period.

3.1.2. Time Series of CH_4 Mixing Ratio
Figure 6 presents the comparisons between observed and simulated time series of CH_4 mixing ratio enhancements over background using the prior and posterior estimates for each flight. The simulated time series using the posterior estimates optimized by the inversion shows better agreement with observations than the simulated time series using the NEI 2005 prior inventory. We calculate the mean bias between observations with the simulations using prior estimates and those using the posterior inventory resulting from the inversion. Mean biases with the posterior estimates distinctly decrease in these studies by 50% to 85% compared with prior estimates. We exclude the overwater segments of the 16 May flight because models did not handle the boundary layer over the water properly [*Angevine et al.*, 2012]. The correlations and the correlation coefficients, R^2, between the observations and the simulated time series are shown in Figure 7 for each flight and each transport model. The slope of the correlations is closer to 1, and R^2 is higher using the posterior estimates compared with the prior estimates for all flights.
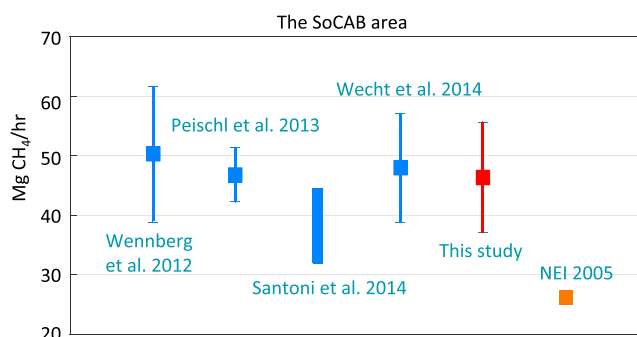

Figure 5. Previous estimates of total emissions of CH_4 in the SoCAB during the CalNex campaign (blue) compared with the estimates from this study. The error bars (1 sigma) present the uncertainties of CH_4 annual emission estimates. The prior estimate of total emissions of CH_4 in the SoCAB from NEI 2005 is shown as well (orange).

3.2. Spatial Distribution of Posterior-Prior Differences
3.2.1. CH_4 and CO Ratios
We use the inversion system and the same six flights as for CH_4 to calculate the posterior inventory of CO for the SoCAB using the updated FLEXPART-WRF version. Our results (~65 kg/s in the SoCAB) are consistent with the CO emissions estimates in *Brioude et al.* [2013a] (68 kg/s). This negligible difference comes from the fact that (i) we clustered grid cells that have small influence on the inversion, and hence, all the grid cells
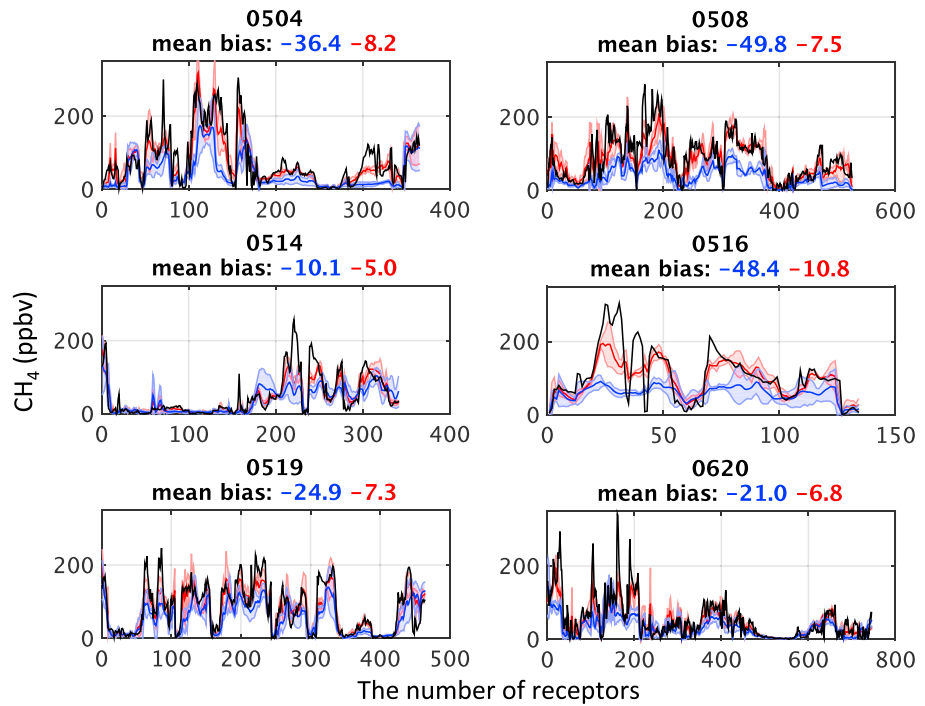
Figure 6. The comparison of observations and models for the time series of the CH$_4$ mixing ratio for NOAA P-3 flights on 4, 8, 14, 16, and 19 May and 20 June 2010. The plot includes the observations (black line), estimates from FLEXPART based on the prior inventory (blue line), and inversion estimates based on the posterior inventory (red line). The shaded areas indicate 1σ variability for the three WRF configurations. Mean biases were calculated between observations and simulations using the prior inventory (blue text) and between the observations and simulations using the posterior (red text). For 16 May flight, we exclude the flight overwater segments because the models did not handle the boundary layer over the water properly.
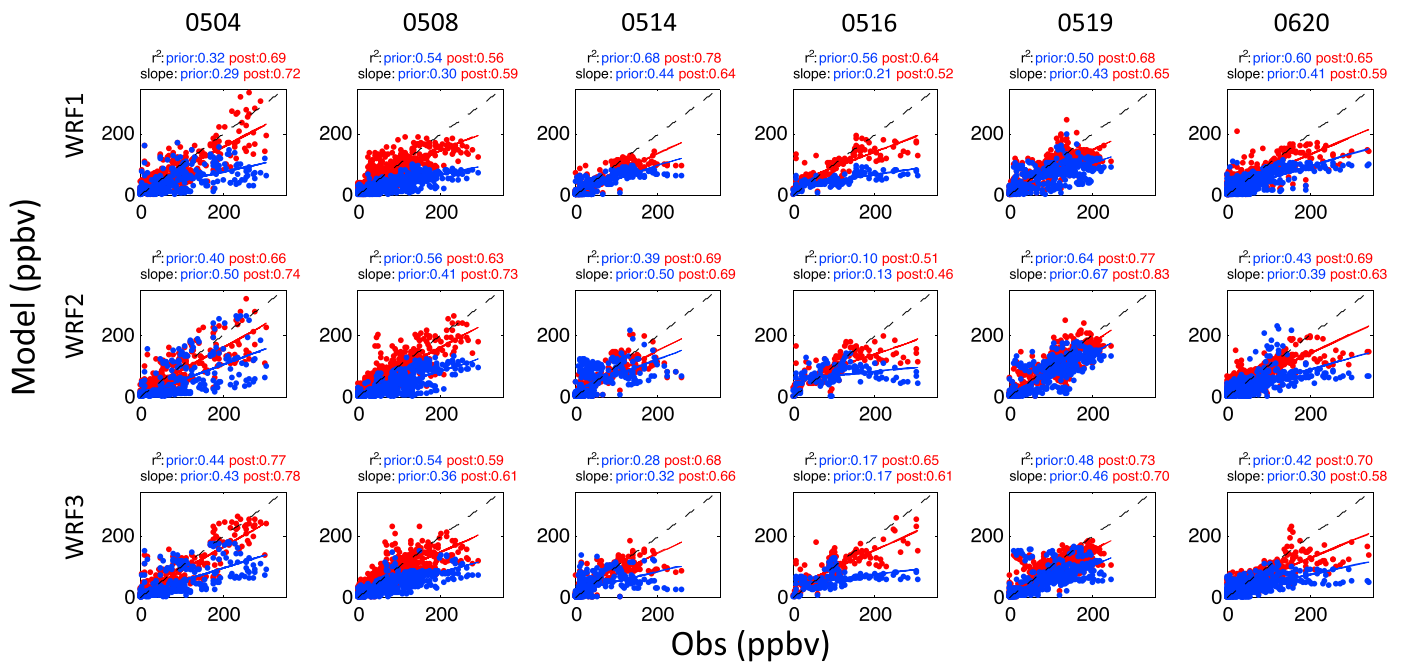
Figure 7. Correlations of the simulated and observed above background CH$_4$ mixing ratio for each flight using the three transport models. The lines indicate the least squares fits to the correlations between observations and simulations with either the posterior inventory (red) or prior inventory (blue). All correlations in the column are significant with $P < 0.05$.
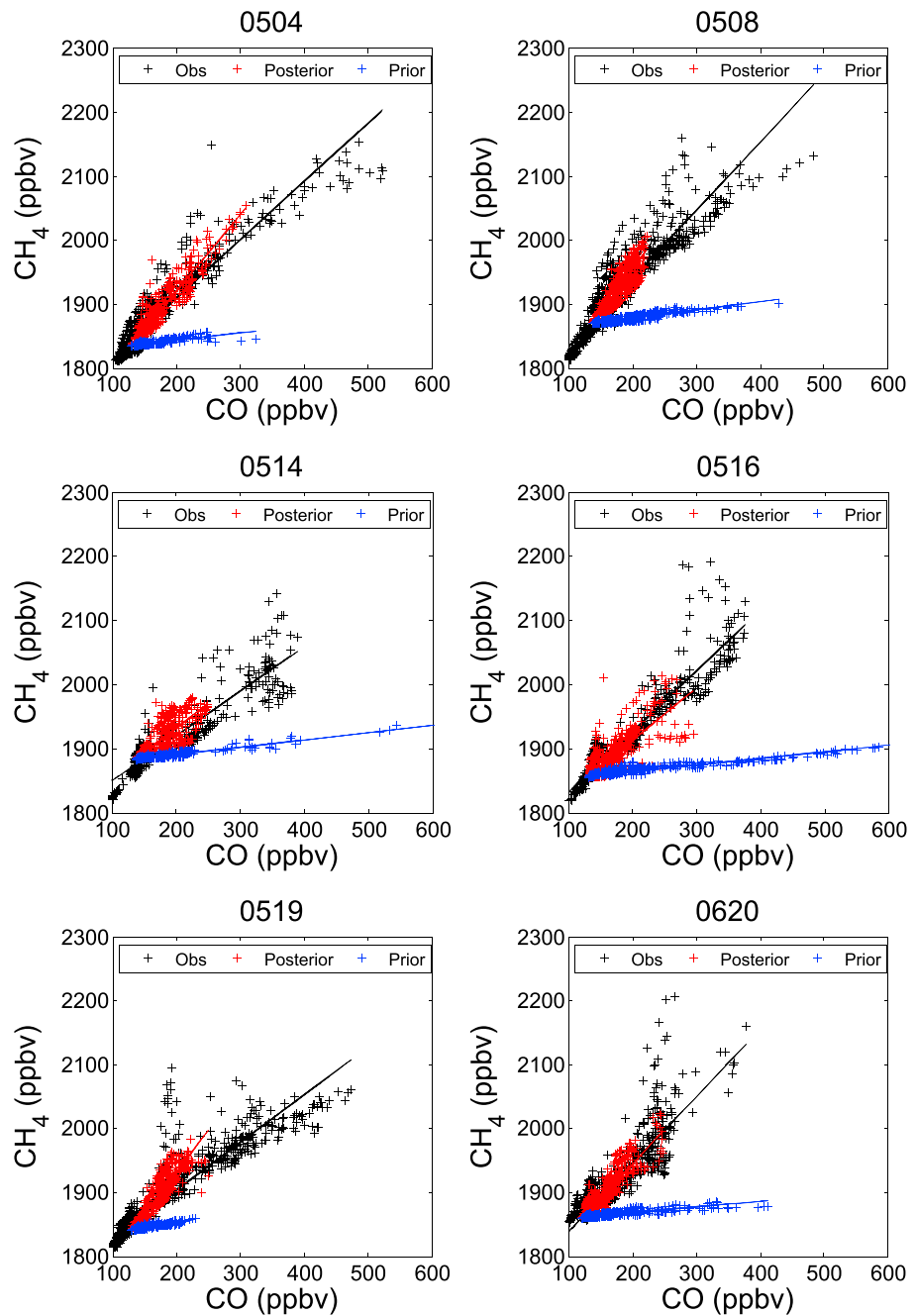
Figure 8. Scatterplot of CH4 versus CO mixing ratios for measurements (black) and simulations, using prior (blue) and posterior (red) emissions for the flights on 4, 8, 14, 16, and 19 May and 20 June. Simulations include results from all data in three WRF configurations. The black dots represent observations of CH_4 and CO mixing ratios, the blue dots show estimates from FLEXPART-WRF based on the NEI 2005 prior inventories of CO and CH_4, and the red dots show FLEXPART-WRF data based on the posteriors from the inversion in this study. The solid lines represent the least squares fit to each set of data, and the dash lines represent 1 standard deviation differences in the slope of the fits.

within the domain are used, while *Brioude et al.* [2013a] limited the inversion on grid cells with significant emission in the prior, (ii) FLEXPART-WRF version has changed with notably a bug fix on the sensible heat flux. The ratio between CH4 and CO, equivalent to the slope of the correlation between the atmospheric mixing ratios of these species, is used to evaluate changes in the spatial distributions of CH4 relative to those of CO between the prior and posterior. Figure 8 presents CH4 and CO correlations and their least
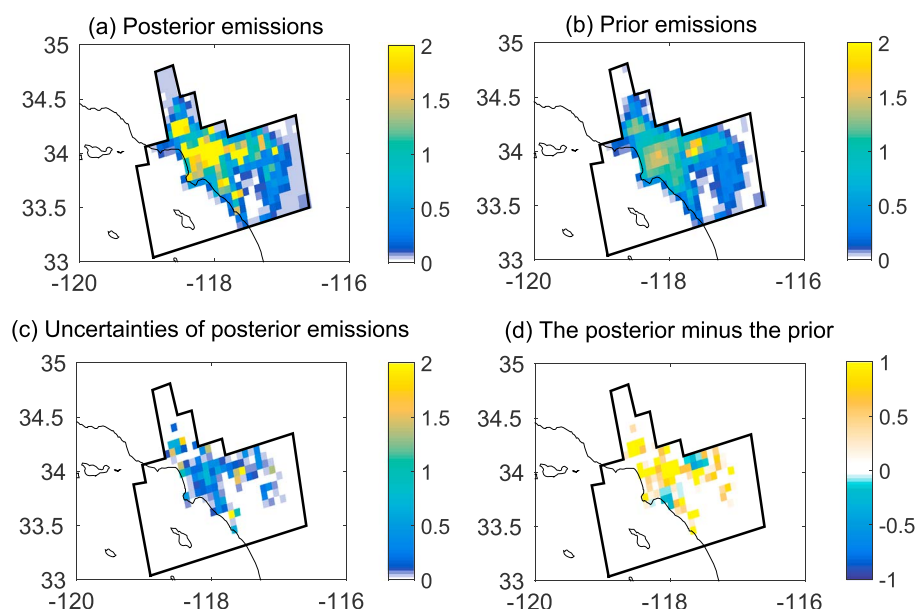
Figure 9. CH_4 surface fluxes (unit: $\mu g\ s^{-1}\ m^{-2}$) from (a) the posterior inventory of our inversion, (b) the NEI 2005 prior inventory, (c) the uncertainties in the posterior inventory, and (d) the difference between the posterior and the prior inventory.

squares fits from the six flights for the observations and simulated by the transport models using the prior and posterior estimates of CH_4 and CO emissions. The slopes between CH_4 and CO are systematically in better agreement with observations using the posterior surface inventory compared with simulations using the prior surface inventory. Slopes between CH_4 and CO from the observations and posterior estimates are in very good agreement.

Figure S2 shows the spatial distribution of surface emission ratio between CH_4 and CO in the prior and posterior inventories. The prior and posterior inventories of CH_4 are shown in Figure 9 and discussed further in section 3.2.2. As shown in Figure 8, CH_4-CO ratios are underestimated in the prior inventory. The CH_4-CO ratio in the prior inventory (Figure S2) is rather homogeneously distributed in the SoCAB, probably due to the missing oil and gas industry sector. In the posterior inventory, the CH_4-CO ratio is heterogeneously distributed, with large ratios where dairies, landfills, and the oil/gas sources are located. The details of these source types are discussed below.

3.2.2. Changes in Spatial Distribution

The spatial distribution of surface fluxes in the posterior and prior inventories and their differences shown in Figure 9 can be used to help quantify emissions from different source sectors. The posterior inventory (Figure 9a) is based on the averaged posterior inventories from each flight and the three transport models. In the SoCAB area, the prior inventory from NEI 2005 (Figure 9b) shows high emissions of CH_4 over Los Angeles County, Orange County, and the Chino area (34°1′N, 117°41′W) where most dairies are located. The uncertainties of the posterior inventory are shown in Figure 9c. There are mostly low values of uncertainties for many grid cells, but relatively high values in the Chino area and the coastal urban area. The posterior inventory presents the same emission patterns as the prior inventory, but with a particularly large increase in CH_4 emissions in parts of the basin dominated by the oil/gas sources and diaries (Figure 9d and Figure 2).

As shown in Figure 2, CH_4 emissions from the dairy sector predominate in the eastern part of the SoCAB and CH_4 emissions of oil/gas sources predominate in the western part of the basin along the coastal urban area. We cannot differentiate the overlapping grids between oil/gas production and distribution sources and landfills. However, the large increase in CH_4 emissions in the western part of the basin (Figure 9d) of CH_4 emissions in the posterior compared to the prior is located in a region where oil/gas production and distribution dominates. This difference is consistent with *Peischl et al.* [2013] who pointed out that those emissions from natural gas distribution and geological seeps could account for the differences between

the bottom-up and top-down results. We estimate the total emissions from oil/gas production, distribution, and landfill sources contribute 39.6 ± 8.1 Mg CH_4/h in the SoCAB, a factor of 1.8 higher than the value in the prior inventory (22.5 Mg CH_4/h), but consistent with estimates (39.0 Mg CH_4/h) in *Peischl et al.* [2013].

The number of overlapping grids between the dairy sources and the other three source types is negligible (Figure 2), which allows us to estimate the total emissions from the dairy sector. We estimate that dairies contribute 5.9 ± 1.7 Mg CH_4/h in the SoCAB, twice the value in the prior inventory (3.1 Mg CH_4/h). This value is higher than the bottom-up estimate from *Peischl et al.* [2013] of 3.6 Mg CH_4/h, but consistent with their top-down estimates of 5.6 ± 2.9 Mg CH_4 /h using a mass balance approach on three P-3 transects downwind of the Chino area during CalNex.

4. Summary and Conclusions

We present the first top-down estimates of CH_4 emissions in the South Coast Air Basin (SoCAB) based on an inverse modeling approach at mesoscale. Annual CH_4 emissions are constrained using in situ measurements from the NOAA P-3 aircraft during the 2010 CalNex campaign over the SoCAB. FLEXPART Lagrangian dispersion model simulated atmospheric transports when coupling with three configurations of WRF runs, the equivalent of three mesoscale transport models. Unlike *Brioude et al.* [2013a], aggregating surface grid cells based on a clustering method is applied to exploit the information content of the inversion to reduce spatial cross correlation between posterior fluxes while allowing computation of the optimal fluxes at a reasonable cost. Simulated CH_4 mixing ratios using the derived CH_4 emissions are in better agreement and better correlation with the measurements ($R^2 = 0.7$) than using the prior inventory ($R^2 = 0.5$). The derived CH4 emission estimates are 46.3 ± 9.2 Mg CH_4/h, in agreement with other recent published observation-based studies.

The inversions are applied to data from individual flights and using the output of the three independent transport models, so our estimated uncertainty includes both the posterior uncertainty and part of the uncertainty from the transport models. However, our uncertainty estimates should be considered as a lower limit. Additionally, we estimate that the total emissions for a given day can be evaluated with data from a single flight with an uncertainty of ~20%. The six flights used in this study are not enough to fully cover the diurnal and day to day emission variations from landfills and feedlots, sources that contribute 44% to the total methane emissions in LA basin [*Peischl et al.*, 2013]. Hence, our posterior emission uncertainty estimates should be considered as a lower limit.

We apply the same inversion with CO measurements to estimate CO surface emissions and analyze CH_4 to CO atmospheric enhancement ratios and surface inventories. The simulated CH_4-CO slopes using the posterior are in good agreement with the observed slopes. The spatial distribution of the CH_4-CO ratios in the posterior inventory is heterogeneous, with higher slopes found in the areas of the basin where most of the oil/gas, landfill, and dairy sources are located. We estimate that dairies in the Chino area contributed 5.9 ± 1.7 Mg CH_4/h, twice the value in the prior inventory (NEI 2005, 3.1 Mg CH_4/h), and consistent with top-down values from *Peischl et al.* [2013] based on a mass balance approach. The oil/gas production and distribution system and landfill sectors together contribute 39.6 ± 8.1 Mg CH_4/h in the SoCAB, a factor of 1.8 higher than the prior inventory, consistent with results in *Peischl et al.* [2013].

We have shown that the mesoscale inverse technique is successful in improving bottom-up CH4 inventories in terms of flux and spatial distribution in a region with complex terrain like the SoCAB area. Our study supports the view that emissions of CH4 in the SoCAB area are greater than expected from population-apportioned bottom-up state inventories and missing or underestimated emissions from dairies, the oil/gas system, and landfills in the SoCAB. As shown in this study, airborne measurements used in a mesoscale inversion could be used to monitor greenhouse gas emissions in a region like the SoCAB. The same technique will be applied to CalNex aircraft measurements over the Central Valley to further improve our knowledge of the statewide emissions of CH_4 and the contributions from different source types.

References

Alvarez, R. A., S. W. Pacala, J. J. Winebrake, W. L. Chameides, and S. P. Hamburg (2012), Greater focus needed on methane leakage from natural gas infrastructure, *Proc. Natl. Acad. Sci. U.S.A.*, *109*, 6435–6440.
Angevine, W. M., L. Eddington, K. Durkee, C. Fairall, L. Bianco, and J. Brioude (2012), Meteorological model evaluation for CalNex 2010, *Mon. Weather Rev.*, *140*, 3885–3906.

Angevine, W. M., et al. (2013), Pollutant transport among California regions, *J. Geophys. Res. Atmos.*, *118*, 6750–6763, doi:10.1002/jgrd.50490.

Angevine, W. M., J. Brioude, S. McKeen, and J. S. Holloway (2014), Uncertainty in Lagrangian pollutant transport simulations due to meteorological uncertainty at mesoscale, *Geosci. Model Dev.*, *7*, 2817–2829.

Bocquet, M., L. Wu, and F. Chevallier (2011), Bayesian design of control space for optimal assimilation of observations. Part I: Consistent multiscale formalism, *Q. J. R. Meteorol. Soc.*, *137*, 1340–1356.

Brandt, A. R., et al. (2014), Methane leaks from North American natural gas systems, *Science*, *343*, 733–735.

Brioude, J., et al. (2011), Top-down estimate of anthropogenic emission inventories and their interannual variability in Houston using a mesoscale inverse modeling technique, *J. Geophys. Res.*, *116*, D20305, doi:10.1029/2011JD016215.

Brioude, J., W. M. Angevine, S. A. McKeen, and E. Y. Hsie (2012), Numerical uncertainty at mesoscale in a Lagrangian model in complex terrain, *Geosci. Model Dev.*, *5*, 1127–1136.

Brioude, J., et al. (2013a), Top-down estimate of surface flux in the Los Angeles basin using a mesoscale inverse modeling technique: Assessing anthropogenic emissions of CO, NO$_x$ and CO$_2$ and their impacts, *Atmos. Chem. Phys.*, *13*, 3661–3677.

Brioude, J., et al. (2013b), The Lagrangian particle dispersion model FLEXPART-WRF version 3.1, *Geosci. Model Dev.*, *6*, 1889–1904.

de Foy, B., Y. Y. Cui, J. J. Schauer, M. Janssen, J. R. Turner, and C. Wiedinmyer (2015), Estimating sources of elemental and organic carbon and their temporal emission patterns using a least squares inverse model and hourly measurements from the St. Louis-Midwest Supersite, *Atmos. Chem. Phys.*, *15*, 2405–2427.

Eastern Research Group (ERG), Inc. (2013), Estimating nonpoint emissions from the oil and gas production sector.

Gao, Z., H. Yuan, W. Ma, J. Li, X. Liu, and R. Desjardins (2011),Diurnal and seasonal patterns of methane emissions from a dairy operation in North China Plain, *Adv. Meteorol.*, *2011*, ID190234, doi:10.1155/2011/190234.

Hegarty, J., R. R. Draxler, A. F. Stein, J. Brioude, M. Mountain, J. Eluszkiewicz, T. Nehrkorn, F. Ngan, and A. Andrews (2013), Evaluation of Lagrangian particle dispersion models with measurements from controlled tracer releases, *J. Appl. Meteorol. Climatol.*, *52*, 2623–2637.

Henze, D. K., J. H. Seinfeld, and D. T. Shindell (2009), Inverse modeling and mapping U.S. air quality influences of inorganic PM2.5 precursor emissions using the adjoint of GEOS-Chem, *Atmos. Chem. Phys.*, *9*, 5877–5903.

Jeong, S., C. Zhao, A. E. Andrews, L. Bianco, J. M. Wilczak, and M. L. Fischer (2012), Seasonal variation of CH4 emissions from central California, *J. Geophys. Res.*, *117*, D11306, doi:10.1029/2011JD016896.

Jeong, S., Y.-K. Hsu, A. E. Andrews, L. Bianco, P. Vaca, J. M. Wilczak, and M. L. Fischer (2013), A multi-tower measurement network estimate of California's methane emissions, *J. Geophys. Res. Atmos.*, *118*, 11,339–11,351, doi:10.1002/jgrd.50854.

Jeong, S., D. Millstein, and M. L. Fischer (2014), Spatially explicit methane emissions from petroleum production and the natural gas system in California, *Environ. Sci. Technol.*, *48*, 5982–5990.

Kim, S.-W., et al. (2011), Evaluations of NOx and highly reactive VOC emission inventories in Texas and their implications for ozone plume simulations during the Texas Air Quality Study 2006, *Atmos. Chem. Phys.*, *11*, 11,361–11,386.

Kort, E. A., J. Eluszkiewicz, B. B. Stephens, J. B. Miller, C. Gerbig, T. Nehrkorn, B. C. Daube, J. O. Kaplan, S. Houweling, and S. C. Wofsy (2008), Emissions of CH$_4$ and N$_2$O over the United States and Canada based on a receptor-oriented modeling framework and COBRA-NA atmospheric observations, *Geophys. Res. Lett.*, *35*, L18808, doi:10.1029/2008GL034031.

Kort, E. A., P. K. Patra, K. Ishijima, B. C. Daube, R. Jiménez, J. Elkins, D. Hurst, F. L. Moore, C. Sweeney, and S. C. Wofsy (2011), Tropospheric distribution and variability of N$_2$O: Evidence for strong tropical emissions, *Geophys. Res. Lett.*, *38*, L15806, doi:10.1029/2011GL047612.

Lee, S.-H., S.-W. Kim, W. M. Angevine, L. Bianco, S. A. McKeen, C. J. Senff, M. Trainer, S. C. Tucker, and R. J. Zamora (2011), Evaluation of urban surface parameterizations in the WRF model using measurements during the Texas Air Quality Study 2006 field campaign, *Atmos. Chem. Phys.*, *11*, 2127–2143.

McKain, K., et al. (2015), Methane emissions from natural gas infrastructure and use in the urban region of Boston, Massachusetts, *Proc. Natl. Acad. Sci. U.S.A.*, *112*, 1941–1946.

Miller, S. M., et al. (2013), Anthropogenic emissions of methane in the united states, *Proc. Natl. Acad. Sci. U.S.A.*, *110*, 20,018–20,022.

Miller, S. M., A. M. Michalak, and P. J. Levi (2014), Atmospheric inverse modeling with known physical bounds: An example from trace gas emissions, *Geosci. Model Dev.*, *7*, 303–315.

Myhre, G., et al. (2013), Anthropogenic and natural radiative forcing, in *Climate Change 2013: The Physical Science Basis. Contribution of Working Group I to the Fifth Assessment Report of the Intergovernmental Panel on Climate Change*, edited by T. F. Stocker et al., Cambridge Univ. Press, Cambridge, U. K., and New York.

Peischl, J., et al. (2012), Airborne observations of methane emissions from rice cultivation in the Sacramento Valley of California, *J. Geophys. Res.*, *117*, D00V25, doi:10.1029/2012JD017994.

Peischl, J., et al. (2013), Quantifying sources of methane using light alkanes in the Los Angeles basin, California, *J. Geophys. Res. Atmos.*, *118*, 4974–4990, doi:10.1002/jgrd.50413.

Pétron, G., et al. (2012), Hydrocarbon emissions characterization in the Colorado Front Range: A pilot study, *J. Geophys. Res.*, *117*, D04304, doi:10.1029/2011JD016360.

Rogelj, J., D. McCollum, and S. Smith (2014), The Emissions Gap Report 2014—A UNEP synthesis report: Chapter 2, United Nations Environment Programme, Nairobi. [Available at http://www.unep.org/publications/ebooks/emissionsgapreport2014/portals/50268/pdf/EGR2014_LOWRES.pdf.]

Ryerson, T. B., et al. (2013), The 2010 California Research at the Nexus of Air Quality and Climate Change (CalNex) field study, *J. Geophys. Res. Atmos.*, *118*, 5830–5866, doi:10.1002/jgrd.50331.

Santoni, G. W., et al. (2014), Evaluation of the airborne quantum cascade laser spectrometer (QCLS) measurements of the carbon and greenhouse gas suite – CO$_2$, CH$_4$, N$_2$O, and CO – during the CalNex and HIPPO campaigns, *Atmos. Meas. Tech.*, *7*, 1509–1526.

Simon, H., et al. (2010), The development and uses of EPA's SPECIATE database, *Atmos. Pollut. Res.*, *1*, 196–206.

Skamarock, W. C., J. B. Klemp, J. Dudhia, D. O. Gill, D. M. Barker, W. Wang, and J. G. Powers (2005), A description of the Advanced Research WRF Version 2 NCAR Tech. Note NCAR/TN-468+STR.

Stohl, A., C. Forster, A. Frank, P. Seibert, and G. Wotawa (2005), Technical note: The Lagrangian particle dispersion model FLEXPART version 6.2, *Atmos. Chem. Phys.*, *5*, 2461–2474.

Stohl, A., et al. (2009), An analytical inversion method for determining regional and global emissions of greenhouse gases: Sensitivity studies and application to halocarbons, *Atmos. Chem. Phys.*, *9*, 1597–1620, doi:10.5194/acp-9-1597-2009.

U.S. Environmental Protection Agency (EPA) (2014), Inventory of U.S. greenhouse gas emissions and sinks: 1990–2012. [Available at http://www.epa.gov/climatechange/Downloads/ghgemissions/US-GHG-Inventory-2014-Main-Text.pdf, last access: 27 May 2015.]

U.S. Environmental Protection Agency (EPA) (2015), Technical support document: Preparation of emissions inventories for the Version 4, 2005-based platform, report, Washington, D. C., 73 pp. [Available at http://www.epa.gov/airtransport/pdfs/2005_emissions_tsd_07-jul2010.pdf, last access: 27 May 2015.]

United States Energy Information Administration (2015), California natural gas gross withdrawals. [Available at http://www.eia.gov/dnav/ng/hist/n9010ca2m.htm, last access: 27 May 2015.]

Wecht, K. J., D. J. Jacob, M. P. Sulprizio, G. W. Santoni, S. C. Wofsy, R. Parker, H. Bösch, and J. Worden (2014), Spatially resolving methane emissions in California: constraints from the CalNex aircraft campaign and from present (GOSAT, TES) and future (TROPOMI, geostationary) satellite observations, *Atmos. Chem. Phys.*, *14*, 8173–8184.

Wennberg, P. O., et al. (2012), On the sources of methane to the Los Angeles atmosphere, *Environ. Sci. Technol.*, *46*, 9282–9289.

Wunch, D., P. O. Wennberg, G. C. Toon, G. Keppel-Aleks, and Y. G. Yavin (2009), Emissions of greenhouse gases from a North American megacity, *Geophys. Res. Lett.*, *36*, L15810, doi:10.1029/2009GL039825.